Review Article **Open Access**

Liu Liu, Mingliang Jin, Yaocheng Shi, Jiao Lin, Yuan Zhang, Li Jiang, Guofu Zhou, and Sailing He*

Optical integrated chips with micro and nanostructures for refractive index and SERS-based optical label-free sensing

DOI 10.1515/nanoph-2015-0015
Received December 29, 2014; accepted May 27, 2015

Abstract: Label-free optical biosensing technologies have superior abilities of quantitative analysis, unmodified targets, and ultrasmall sample volume, compared to conventional fluorescence-label-based sensing techniques, in detecting various biomolecules. In this review article, we introduce our recent results in the field of evanescent-wave-based refractive index sensing and surface enhanced Raman scattering (SERS)-based sensing, both of which are promising platforms for label-free optical biosensors. First, silicon-on-insulator (SOI) nanowire waveguide and metallic surface plasmon resonance (SPR)-based refractive index sensing are discussed. In order to improve the detection limit, phase interrogation techniques are introduced to these types of sensors based on prism-coupled SPR and SOI microring resonators. A detection limit in the order of 10^{-6} refractive index unit is achieved. Detection of 16.7 pM anti-IgG is also demonstrated based on the SPR devices. Second, SERS substrates based on various nanometallic structures are discussed. Metallic nanowire arrays and inverted nanopyramids and grooves with a thin metal surface are fabricated based on anisotropic wet-etching of silicon substrates. Both structures have demonstrated a Raman signal enhancement on the order of 10^7. In order to improve the extraction efficiency of the Raman signal at a high wave number, a nano-bowtie array substrate is fabricated, which exhibits double resonances at both the excitation wavelength and the desired Raman scattering wavelength. Experimental results have shown that this double-resonance structure can further enhance the received Raman signal, as compared to conventional SERS substrates with only one resonance at the excitation wavelength.

1 Introduction

Biosensors, which provide the ability to detect and study the presence of certain biomolecules from body fluids or environmental samples, have been widely used in applications such as disease diagnostics, drug development, food safety, and environmental monitoring [1–4]. Because of the complexity of the biomedical samples, an ideal biosensor should have a low detection limit and a high specificity. The detection limit can be defined as the minimal quantity of the target analyte that can be detected by the sensor. The specificity means that the sensor should only be sensitive to the target analyte, while not responsive to other materials that might reside in the sample with higher quantities (orders of magnitude). In addition, multiplexability, high throughput, large dynamic range, and low sample volume are also important characteristics of a modern biosensor [5]. In general, the technologies behind a biosensor can be categorized into labeled detection and label-free detection. The former case is an indirect method, which relies on

Liu Liu, Yuan Zhang: SCNU-ZJU Joint Research Center of Photonics, Centre for Optical and Electromagnetic Research, South China Academy of Advanced Optoelectronics, Science Building No. 5, South China Normal University, Higher-Education Mega-Center, Guangzhou 510006, China
Mingliang Jin, Guofu Zhou: Institute of Electronic Paper Displays, South China Academy of Advanced Optoelectronics, Science Building No. 5, South China Normal University, Higher-Education Mega-Center, Guangzhou 510006, China
Yaocheng Shi, Jiao Lin, Li Jiang: Centre for Optical and Electromagnetic Research, JORCEP [Sino-Sweden Joint Research Center of Photonics], Zhejiang Provincial Key Laboratory for Sensing Technologies, East Building No. 5, Zijingang Campus, Zhejiang University, Hangzhou 310058, China
***Corresponding Author: Sailing He:** SCNU-ZJU Joint Research Center of Photonics, Centre for Optical and Electromagnetic Research, South China Academy of Advanced Optoelectronics, Science Building No. 5, South China Normal University, Higher-Education Mega-Center, Guangzhou 510006, China; Centre for Optical and Electromagnetic Research, JORCEP [Sino-Sweden Joint Research Center of Photonics], Zhejiang Provincial Key Laboratory for Sensing Technologies, East Building No. 5, Zijingang Campus, Zhejiang University, Hangzhou 310058, China; Email: sailing@jorcep.org

BY-NC-ND © 2015 Liu Liu *et al.*, published by De Gruyter Open.
This work is licensed under the Creative Commons Attribution-NonCommercial-NoDerivs 3.0 License.

labeling the target molecule with, for example, a specific fluorescence tag [6]. The presence and the concentration of the target molecule can then be studied through measuring the fluorescence intensity of the modified sample. Despite being successfully adopted nowadays, such as in ELISA (enzyme-linked immunosorbent assay) tests [7], labeled detection technology has several drawbacks, such as laborious and expensive processes [8], difficulties in quantitative and real-time analysis [9], and complexities in multiplexed sensing [10, 11]. On the other hand, in the label-free detection method, the target molecule is unlabeled, and it is studied directly through an optical, an electrical, or a mechanical transducer [12]. This type of unmodified and direct detection is not only easy to perform, but also facilitates a quantitative and kinetic measurement of molecules and the interactions between them. Highly multiplexed sensing chips with an ultrasmall sample volume are also made possible by state-of-the-art integration technologies [13]. There exist many different label-free technologies [8, 12–16]. In this review, we will focus on two types of optical label-free biosensor chips based on, respectively, evanescent-wave-based refractive-index sensing [8, 13] and surface enhanced Raman scattering (SERS) [15, 16].

An evanescent wave is an exponentially decaying optical field near the interface of two materials. The optical fields of a guided mode in the cladding layer of an optical waveguide are a typical evanescent wave [17]. In the evanescent-wave-based refractive index sensor, the target analyte is immobilized at the surface of a waveguide core through specific biomolecular interactions, which will result in a refractive index change of the cladding. The evanescent wave of a guided mode will feel this change, as well as the effective index of the guided mode, which will then be measured as the sensor response by using interference or resonance [18]. Using various interference structures, such as Mach-Zehnder [19] or Young interferometers [20], detection limits of 10^{-7}–10^{-9} have been demonstrated. However, such a small detection limit is realized through a long interaction length between the optical mode and the analyte, typically in the order of millimeter or centimeter. In this case, the footprint of a single sensor device is large, which hampers sensing applications that require a low sample volume or a high throughput. It is also difficult to implement in the form of a large array. Resonant structures, on the other hand, provide not only a high sensitivity, but also the potential for densely integrated arrays or matrixes for multiplexed sensing [13, 21]. The most common and well-developed optical evanescent-wave-based resonant sensor is the surface plasmon resonance (SPR) device. The surface plasmon mode near a

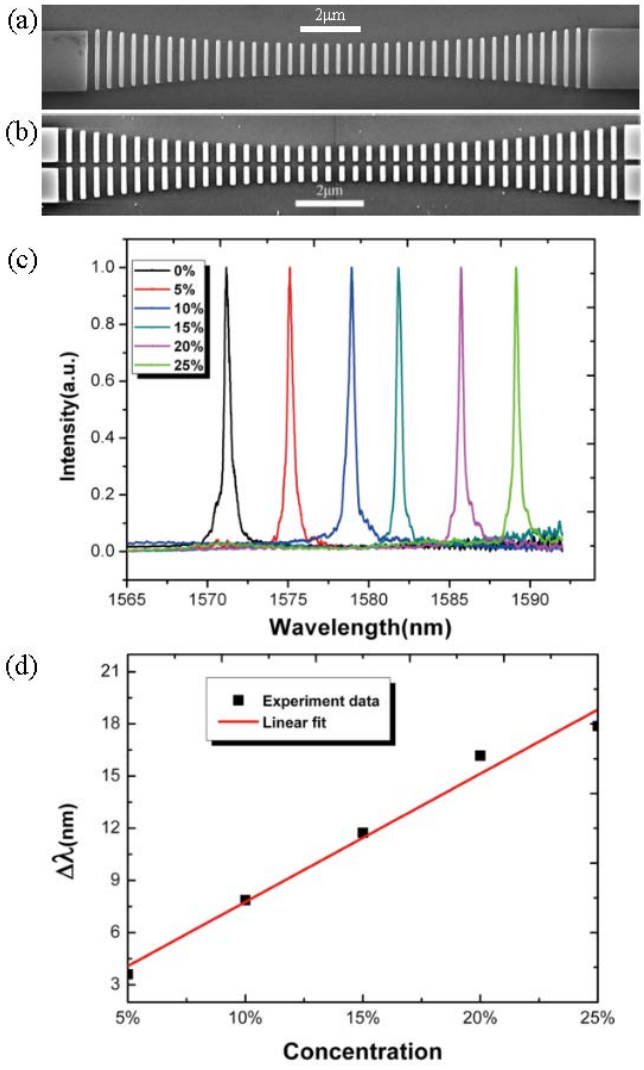

Figure 1: Images of the fabricated PhC cavity devices without (a) and with (b) slots. Measured transmission responses (c) and resonant wavelength shifts (d) of the slotted device covered under aqueous NaCl solutions with different concentrations. Adapted from Ref. [25].

metal-dielectric interface exhibits a predominant evanescent wave in the dielectric [22], which will greatly enhance the sensor response [21]. In recent years, highly integrated waveguide systems, such as those based on silicon-on-insulator (SOI) platforms, have drawn significant attention [23]. A sensor chip made on an SOI wafer can integrate hundreds of individual sensors, each of them with a small effective sensing area, which facilitates a small sample volume and highly multiplexed lab-on-a-chip system [13]. We have demonstrated an evanescent-wave-based nanosensor using a slotted SOI photonic crystal cavity with a parabolic-width stack. A sensitivity of 410 nm/RIU (refractive index unit) and a sensing footprint of 16.8 × 2.5 μm^2 have been achieved [24, 25]. As mentioned above, differ-

ent interrogation approaches have been employed in order to measure the effective index change of the guided mode in an evanescent-wave-based sensor. The most common approaches are angular interrogation and wavelength interrogation for prism-coupled SPR sensors and integrated waveguide sensors, respectively [8]. We demonstrated that using phase interrogation instead can help to obtain an enhanced and more stable sensor response. A detection limit on the order of 10^{-6} RIU has been achieved for sensors based on SOI microring resonators and prism-coupled SPR [26–28].

SERS was discovered about 40 years ago [29], and has become a popular tool for molecular qualification, due to its ultrahigh sensitivity (down to a single molecule) and its high selectivity (capable of identifying analytes in a mixture without separation). Nowadays, the optical field enhancement on the metallic surface generated by localized SPRs and the chemical charge effect is commonly accepted as two major theoretical bases for understanding SERS. When the optical field, generated by localized SPRs, on metallic surfaces is limited in a very narrow volume such as nanogaps [30–33], nanocrevices [34–36], and nanoslits [37–39], the optical field in the spaces will be extremely enhanced. This effect is called the coupling effect [40], and the effective area is called a "hot spot" [41]. This phenomenon will dramatically enhance the Raman scattering signal of the molecule, which is localized in the "hot spot" area [42]. In 1997, for the first time, SERS was implemented as a label-free technology for single molecule detection using silver nanoparticles [43]. Recently, there has been more interest seen toward realizing large-area, reproducible, and uniform SERS substrates. We developed INPGs and nanowire array structures for SERS with exceptional enhancement factor (EF), signal uniformity, and easy fabrication [44, 45]. Novel double-resonant nanostructures for enhancing not only the excitation light in SERS but also the scattered Raman signal light were also demonstrated [46].

2 Evanescent-wave-based refractive index sensing chips with microresonant structures

2.1 Conventional sensing scheme based on intensity signals

It is known that in an ideal and lossless resonant structure light can only exist at the resonant condition, for example, a single wavelength. However, such an ideal resonance is not practical since it cannot be excited. When the resonant structure is coupled to the outside world through, for example, a waveguide [13] or a prism [21], this resonance can then be excited and measured. A resonant peak or dip will appear in measured intensity spectral curve. Because of this coupling loss, as well as the possible intrinsic losses resulting from radiation or material absorption, the resonance would be no longer at a single wavelength, but of a broader shape as shown in Fig. 1. When the refractive index of the analyte changes, the resonant condition will shift correspondingly, which can then be used as the sensor response. Table 1 lists the performance of some resonance-based refractive index sensors.

In prism-coupled SPR devices, where the SPR is excited when the wave vector of the excitation light matches the propagating constant of the surface plasmon mode, that is, the resonant condition, normally through a high-refractive-index prism [47–49], the sensor response can usually be extracted through direct intensity measurement, or intensity spectrum by scanning the incident wavelength or angle. For improved intensity-interrogated SPR sensors, the detection limit has reached 10^{-6} RIU. Homola's group utilized polarization contrast with a spatially resolved functionalization combined with SPR imaging on spatially patterned multilayers to achieve a lower detection limit of 2×10^{-6} RIU [50]. Lechuga's group combined the magnetoactivity of magnetic materials with SPR in a multilayer substrate to realize a detection limit of 5×10^{-6} RIU [51]. For angular-interrogated SPR sensors, Thirstrup's group integrated holographic optical elements and utilized a diffractive grating to produce a parallel beam with an angular spectrum detected by a photodetector [52]. Such a system can resolve refractive index changes down to 5×10^{-7} RIU. For improved wavelength-interrogated SPR sensors, Homola's group designed a platform with wavelength modulation and parallel channel architecture, where the polychromatic light reflected from different channels can be collected by different output collimators [53]. More recently, a detection limit of 2.5×10^{-8} RIU has been attained by exciting a long range SPR and combing superluminescent diode with polarization-maintaining fibers [54].

Normally, for evanescent-wave sensors based on resonant devices, their ability to detect small refractive index changes, that is, the detection limit as mentioned above, can be expressed in terms of the ratio of the resonant wavelength change over the corresponding refractive index change, that is, nm/RIU (normally referred as sensitivity), as well as the sharpness of the resonance itself, typically described as the Q-factor [55]. To obtain a large

Table 1: Performance comparison of some resonance based refractive index sensors using SOI and SPR structures. N.A.: not described in the paper.

Resonance	Technology	Sensitivity	Detection limit
SPR	Angular interrogation [52]	2.269 rad/RIU	5×10^{-7} RIU
	Wavelength interrogation [54]	57000 nm/RIU	2.5×10^{-8} RIU
	Phase interrogation using PZT [74]	3173 rad/RIU	5.5×10^{-8} RIU
	Phase interrogation using PPM [27]	1183 rad/RIU	7.6×10^{-7} RIU
Ring or disk resonator based on SOI	Single ring resonator [56]	70 nm/RIU	10^{-5} RIU; 10ng/mL
	Single ring resonator using slot waveguide [68]	298nm/RIU	4.2×10^{-5} RIU
	Double ring resonators using Vernier effect [57]	2169 nm/RIU	8.3×10^{-6} RIU
	SOI ring array [60]	163 nm/RIU	7.6×10^{-7} RIU; 60 fM
	Cascaded rings using WDM interrogation [61]	135nm/RIU	20pM
	Single ring using phase interrogation [26]	6000 rad/RIU	2.5×10^{-6} RIU
PhC cavity based on SOI	Cascaded PhC cavity [66]	~140 nm/RIU	7×10^{-5} RIU
	2D slotted PhC heterostructure cavity [69]	1500 nm/RIU	7.8×10^{-6} RIU
	Parabolically modulated 1D slotted PhC cavity [25]	410 nm/RIU	N.A.

wavelength change for a certain refractive index change, the majority of the electric field should be confined to the areas with the target analyte. In order to distinguish this wavelength change, a high Q-factor resonator is always desired. The SPR devices discussed above can provide a high sensitivity due to the large overlap of the optical mode with the analyte. However, the Q-factor of the SPR is normally low (< 1,000) [47–54] due to the high absorption loss resulting from the metal. All-dielectric resonant structures, which could intrinsically avoid this high absorption loss, have drawn great attentions in the recent years.

Microring or microdisk resonators are typical forms of such structure, which facilitate mass production, as well as multiplexed sensing in an array. Based on the SOI platform, De Vos et al. demonstrated an integrated chemical and biosensor using a 5 μm-radius ring addressed by two bus waveguides [56]. A cladding refractive index sensitivity of 70 nm/RIU was initially reported with a lower detection limit of 10^{-5} RIU. By functioning the silicon surface for biosensing, avidin molecule with a concentration of 10 ng/mL is detectable by the device. Lately, the same group employed two SOI ring resonators with slightly different radii and the Vernier effect to increase the sensitivity to 2169 nm/RIU [57]. The detection limit of this double-ring structure was expected to reach 8.3×10^{-6} RIU. The SOI ring adopted in the previous example was of a moderate Q-factor (about 20,000). The record high Q-factor is, however, realized in the toroidal-shaped disk resonator made of silica [58, 59]. Using a selective reflow process, an ultrasmooth surface can be achieved on the resonator, which pushed the Q-factor up to the order of 10^8 with a disk of 80 μm radius [58]. With this device, a detection limit of 5 aM for interleukin-2 cytokine, as well as single-molecule detection, was demonstrated [59]. However, this type of toroidal resonator was addressed through a tapered fiber, which is still not a fully integrated solution. Besides improving the Q-factor, researchers have also developed different ways to remove or compensate the noise of the intensities signals, which accounts for the major obstacle to further improve the detection limit of an conventional waveguide-coupled ring resonator. Iqbal et al. fabricated a sensor chip with 32 SOI rings as the sensing elements, where 24 rings were used for detecting different biomolecule and the rest eight for referencing [60]. A complex rapid scanning and interrogating platform was developed in order to address all the rings in real-time. With this scheme, detection limits of 7.6×10^{-7} RIU and 60 fM were achieved for bulk refractive index sensing and biomolecule sensing of streptavidin, respectively. On the other hand, Xu et al. adopted the wavelength multiplexing properties of the ring resonators [61]. By cascading rings of slightly different radii, five rings can be addressed at dif-

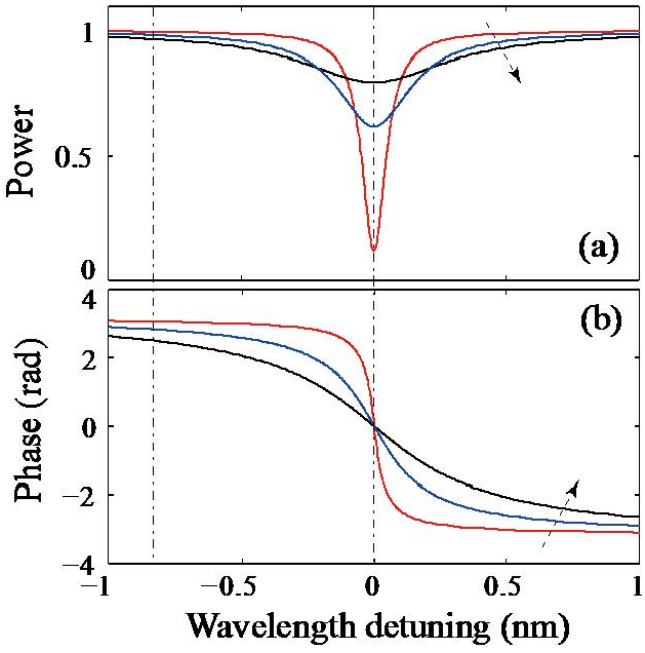

Figure 2: (a) Power and (b) phase responses of an all-pass ring resonantor under the overcoupled condition. For the different curves shown here, the coupling coefficients between the ring and the bus waveguide increase along the direction of the dashed arrow.

ferent wavelengths with only one bus waveguide, which would potentially simplify the measurement system. A detection limit of 20 pM for proteins was demonstrated.

While the footprint of a ring resonator is still not compact (10 μm–100 μm), PhC, which consists of a periodic arrangement of materials with different dielectric constants, allows the realization of resonators where light is localized on scales comparable to the wavelength. Because of the development of fabrication technologies, PhC cavities with high quality factors up to 10^6 have been demonstrated [62], with small mode volumes in the order of a cubic wavelength. Recently, one-dimensional PhC nanocavities [63–65] have attracted considerable interest due to properties such as their comparable quality factor with conventional two-dimensional PhCs, easy coupling with waveguides, and a small footprint. Mandal et al. used a serial of one-dimensional PhC cavities coupled to one bus waveguide based on SOI as a multiplexed sensor structure [66]. These PhC cavities have a slightly different cavity lengths, and thus the sensor elements can be addressed with different wavelengths, which is similar to the ring-resonator case discussed in Ref. [61]. Yet, the footprint of such a PhC cavity is more than two orders smaller as compared to that of the ring. Although the Q-factor of the PhC cavity is not very high (~3000), a bulk refractive index detection limit of 7×10^{-5} RIU was still demonstrated. We designed a one-dimensional PhC stack mode-gap cavity with a high Q-factor [24]. It consists of a simple periodic array of dielectric blocks. The widths of the dielectric blocks are quadratically modulated in order to introduce a defect into the photonic bandgap, as shown in Fig. 1(a). The resonating mode can be optimized to be located close to the air-band. Thus, the majority of the optical field is distributed in the low-index cladding. The parameters for the cavity are optimized to achieve a high sensitivity while maintaining a high Q-factor. The measurements showed that a sensitivity of 269 nm/RIU together with a Q-factor as high as 27,000 can be achieved [24].

As compared to the SPR devices, the sensitivity of a typical integrated resonator on SOI is still low, since the majority of the optical mode still resides in the high-refractive-index core material. Only a small portion of the mode, that is, the evanescent field, interacts with the cladding analyte. Through employing a slot waveguide structure, the evanescent field portion can be greatly enhanced in the low-refractive-index slot region [67]. A stronger light-analyte interaction can therefore be obtained. Claes et al. introduced a slot-waveguide based ring resonator on the SOI platform [68]. A 4-time and 3.5-time improvement for the bulk refractive index sensitivity and surface sensitivity to protein with respect to the normal SOI ring resonator was obtained experimentally, respectively. Combining the slot waveguide and photonic crystal structures, it is possible to construct a high-sensitivity resonant sensor with a small footprint. By using such a structure, Di Falco et al. designed a heterostructure cavity with a Q-factor of 50,000. A ultrahigh bulk refractive index sensitivity of 1500 nm/RIU was experimentally demonstrated [69]. However, such a high measure is partially due to the wetting of different solutions, which is difficult for practical applications.

We have also introduced the slot-waveguide structure in the aforementioned one-dimensional PhC cavity, as shown in Figure 1(b) [25]. The slotted stack cavity is formed by introducing a slot between two periodic arrays of dielectric stacks. The majority of the optical field is distributed in the slotted low-index area, and the light interaction with the analytes has been enhanced. By employing a parabolically modulated width stack without any reflected mirror, high Q-factor of 9200 has been achieved. As compared to the cavity discussed in Ref. [69], the present slotted PhC cavity, due to the open geometry, makes the analyte access the slot area more easily, which effectively avoids the wetting problem. The measured transmission spectra for the cavity covered by NaCl solutions with different concentrations exhibit a sensitivity of 410 nm/RIU, which is 1.5 times the sensitivity for the one without slots. The small foot-

print of the device ($16.8 \times 2.5\ \mu m^2$) also suggests a strong potential in on-chip biochemical sensing arrays.

2.2 Phase-interrogated resonance-based sensors

As discussed in the above section, the wavelength or angular interrogation method is conventionally used to measure the response in a resonance-based evanescent-wave sensor, which relies on the measurement of the intensity signal. This method is vulnerable to alignment accuracy and stability, wavelength scanning accuracy and repeatability, the resolution of the spectrum analyzer, etc., which will give rise to noise in the measured wavelength response [60]. Besides the intensity characteristics, it is known that the phase information around a resonance can also be used as the sensor signal. Figure 2 shows the intensity and phase transmission spectrum of an all-pass ring resonator under overcoupled regime [70]. One can find that the phase response of such a resonance shows a steep transition around the resonant wavelength. Such a phase-interrogation method can efficiently shield the intensity noise sources and provide an ultrastable reading of the sensor response, and hence a better detection limit. This type of sensing scheme has been developed and applied to the SPR-based sensors. Wu et al. combined acousto-optomodulators (AOMs) with a common path heterodyne interferometer [71]. One of the AOMs can be excited at 40 MHz and another at 40.06 MHz in order to induce two linearly orthogonally polarized beams with a frequency difference of 60 kHz. After the two beam emerging into the heterodyne interferometer, the phase of SPR can be monitored. Yuan et al. studied a photoelastic modulator (PEM) based on ellipsometry [72]. Using the first and second harmonics of the modulated frequency, the polarization parameters and ellipse orientation angle can be measured directly. Shao et al. employed a liquid crystal modulator (LCM) in a wavelength-multiplexing phase-sensitive system [73]. LCM can be used to modulate the optical retardation for phase dithering, and the intensity response of the sensor surface can be captured simultaneously. Wu et al. employed the piezoelectric transducer (PZT) into the Mach–Zehnder configuration to calculate the phase of SPR [74]. The PZT of the reference mirror can be driven by a sawtooth wave oscillating at 1.1 Hz, which produces aperiodic linear phase shift of more than 10 interference fringes. The phase of SPR was then monitored in real-time with a correlation software program. The bulk refractive-index detection limit of this scheme reached 5.5×10^{-8} RIU. Law's group has integrated nanoparticles and immunoassay sensing into phase-interrogated SPR system to detect antigen in the fM range [75].

In the above phase-interrogated SPR systems, the adopted phase modulators, including AOM, PZT, LCM, and PEM are expensive, and easily influenced by temperature and vibration disturbance. Recently, we have proposed a novel phase interrogation method employing a prism phase modulator (PPM) to modulate the polarization statue and the phase retardation of the incident light for SPR sensing [27, 28]. Compared with these modulators, PPM can offer high precision, strong stability, and low prices, which is desirable for the commercialization of SPR devices. The PPM utilizes an uncoated rotational rhombic prism to modulate the phase difference between p- and s-polarized light with total internal reflection eight times, as shown in Fig. 3. The total phase difference φ_m can be calculated by subtracting the phase shift of p-polarized light propagating through the rhombic prism with that of s-polarized light [27, 28]. The phase difference φ_m can be modulated by scanning the incident angle θ on the prism. After modulation, the light is coupled into the SPR microfluidic chip through a coupling prism, and the p-polarized light would excite the SPR at the surface of the Au film of the chip at a certain incident angle, and this angle will shift when the refractive index of the media attached to the Au film changes. In this case, the reflected p-polarized light would be accompanied with an intensity attenuation together with a steep phase jump, similar to the case in the ring resonator as discussed in the previous section. On the other hand, the s-polarized light will be reflected normally by the Au film, showing a high reflection intensity and a smooth phase response. This s-polarized light is used as a reference similar to the laser wavelength lying away from the resonance discussed in the previous section. To extract the phase information of the SPR, the reflected p- and s-polarized light beams would interfere through a linear polarizing analyzer. The detected intensity signal I can be expressed as $I = I_p \cos^2\theta_p + I_s \cos^2\theta_s + 2\cos\theta_p \cos\theta_s \sqrt{I_p I_s} \cos(\varphi_{spr} + \varphi_m)$, where, I_p and I_s are the intensities of the reflected p- and s-polarized light, respectively, θ_p and θ_s are the angles to the polarizer axis of the linear polarizing analyzer for the corresponding polarizations, and φ_{spr} is the phase induced by the SPR to the p-polarized light and is measured as the sensor response. The detected intensity signal I exhibits a typical sinusoidal response as φ_m is scanned (through scanning θ), and φ_{spr}, that is, the phase of the sinusoidal response, can be extracted through a curve fitting operation.

Two kinds of integrated microfluidic chips with SPR arrays were fabricated in order to fulfill the high throughput and multiplexed sensing requirement. One is com-

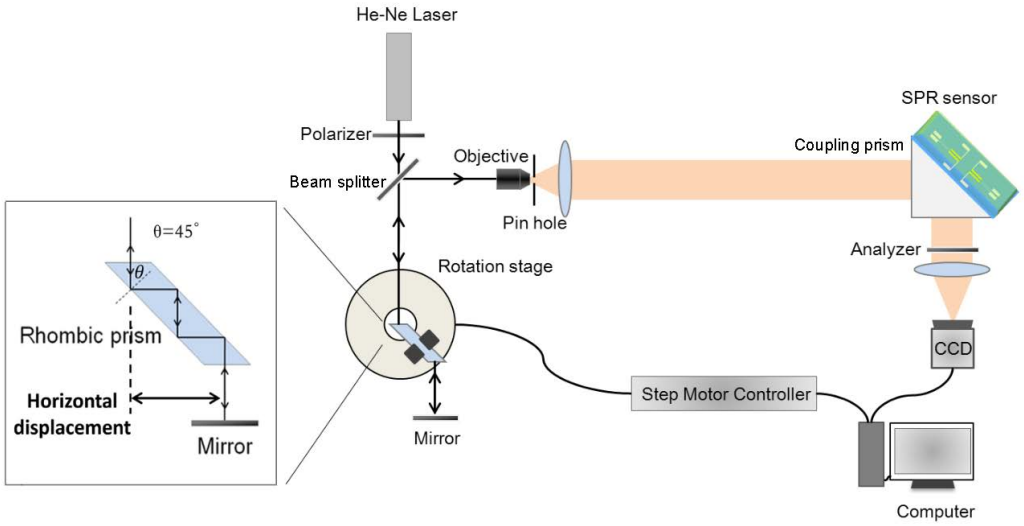

Figure 3: Schematic diagram of PPM-based phase-sensitive SPR sensing system. The PPM is placed on a rotation stage.

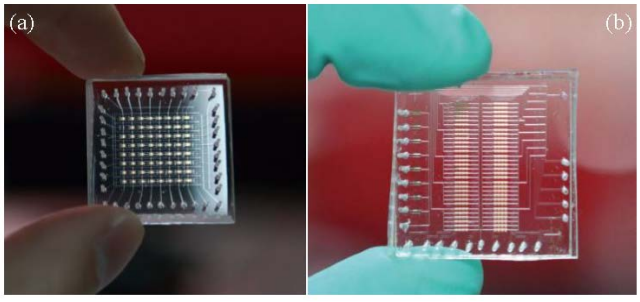

Figure 4: (a) 8 × 8 microfluidic chip with independent channels. Taken from Ref. [27]. (b) Logic microfluidic chip.

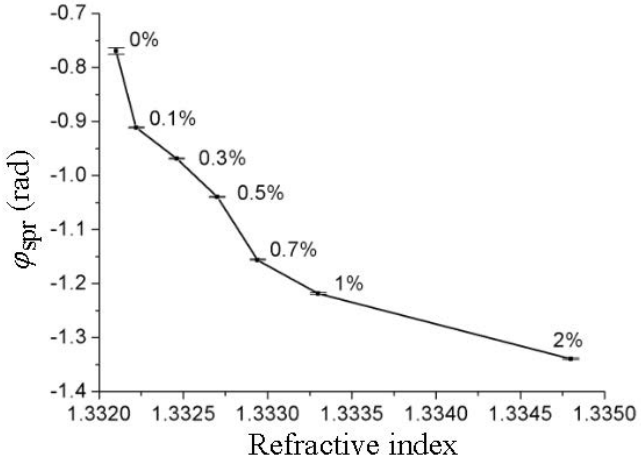

Figure 5: The mean values of the sensor response φ_{spr} with different glycerine solutions. Adapted from Ref. [27].

posed of eight vertical channels and eight horizontal channels, as shown in Fig. 4(a). Each channel is connected to an inlet opening and an outlet opening. A sensing array with 8 × 8 SPR sensing spots (size 0.5 × 0.8 mm^2 each) made of Au is situated in the intersections of the vertical and horizontal channels, which are independently controlled by microvalves actuated pressure (~0.15 MPa). The other chip integrates 240 Au spots (size: 0.4 × 0.4 mm^2 each), one inlet channel, one outlet channel, 10 main flow channels, 60 minor flow channels, 5 main microvalves, and 8 minor microvalves together, as shown in Fig. 4(b). By utilizing the concept of a fluidic logic gate, one individual channel can be selected to work while the other channels are closed when applying pressure to the three main microvalves and four minor microvalves. As a result, 16 different samples can be analyzed simultaneously on the sensing chip.

The detection limit test was carried out on the 8 × 8 microfluidic chip by choosing two vertical channels as a probe channel and a reference channel, respectively. Glycerine solutions with gradient concentrations from 0% to 2% were injected into the probe channel sequentially, while deionized water was injected into the reference channel. As a result, the sensor response φ_{spr} decreases gradually when the concentration is changed from 0% to 2%, as indicated in Fig. 5. Since the initial coupling angle for exciting SPR was adjusted for the case when deionized water is in the probe channel, the SPR signal decreases most sharply when the concentration of the glycerine solution is low. The maximal sensitivity based on this PPM-based phase interrogation was 1.183×10^3 rad/RIU, which is associated with a detection limit of 7.61×10^{-7} RIU [27].

To demonstrate the biomolecular label-free sensing ability of the SPR microfluidic chips, we further tested the detection of several proteins, that is, anti-Angiogenin

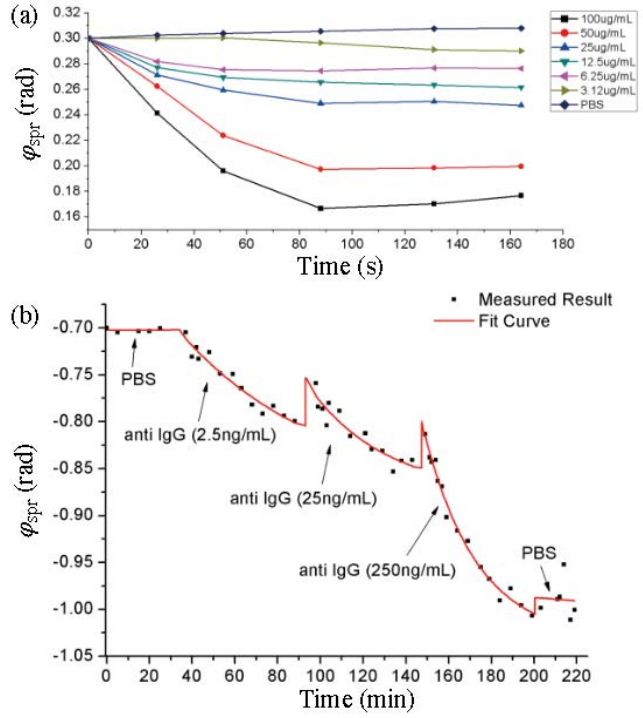

Figure 6: Kinetic results of the sensor response φ_{spr}. (a) The interaction between Angiogenin and anti-Angiogenin. Adapted from Ref. [27]. (b) The interaction between bovine IgG and anti-bovine IgG. Adapted from Ref. [28].

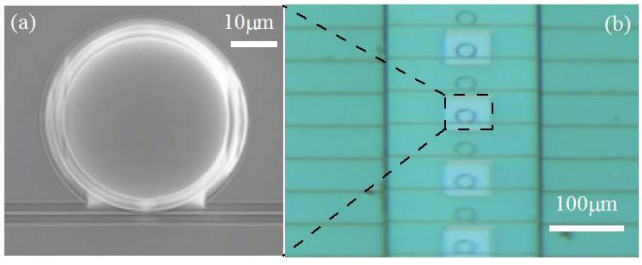

Figure 7: (a) Picture of a fabricated SOI ring resonator. (b) Image of a finished sample with a microfluidic channel attached.

and anti-bovine IgG. In the first case, angiogenin was self-assembled on the Au spots. After that, the horizontal microvalves were closed and the vertical microvalves were opened to allow anti-angiogenin solutions with different concentrations of 3.12, 6.25, 12.5, 50, and 100 μg/mL to flow in separate channels. As indicated in Fig. 6(a), the sensor response φ_{spr} decreased after the injection of anti-angiogenin solution due to the conjugation of anti-angiogenin and angiogenin. Anti-angiogenin solutions with different concentrations can be clearly distinguished by reading the sensor response φ_{spr} after reaching their equilibriums.

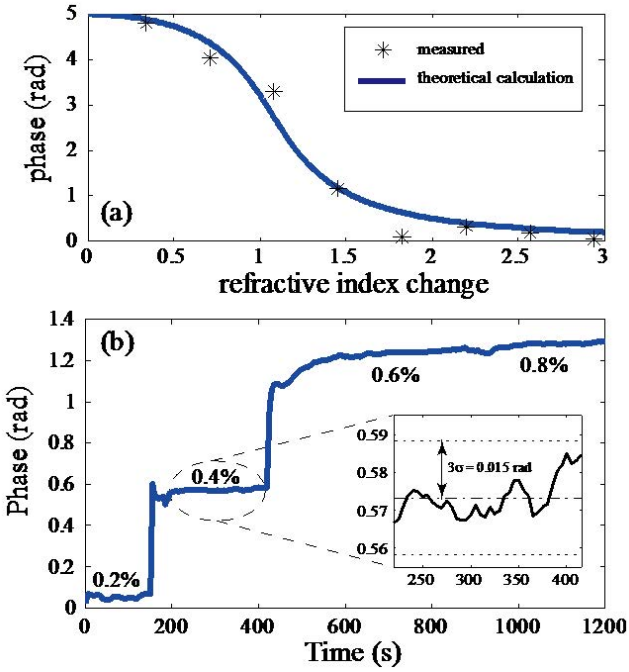

Figure 8: (a) Theoretically calculated and measured phases with respect to the refractive index change (from deionized water) of the cladding materials. (b) Kinetic response of the phase readings. Numbers marked beside the curve indicate the corresponding mass concentrations of the NaCl solutions flowing through the sample. The inset shows a zoomed-in plot of the section marked with the dashed ellipse indicating the noise of the measurement. Adaped from Ref. [26].

For the detection of anti-bovine IgG, the Au spots were first assembled with bovine IgG. After functionalization, anti-IgG solutions with concentrations of 2.5 ng/mL, 25 ng/mL, and 250 ng/mL were injected into the probe chamber sequentially in the same channel. Because of the combination between IgG and anti-IgG, the sensor response φ_{spr} decreased substantially after injecting the anti-IgG solution, and the decreasing speed became faster while the concentration of anti-IgG increased, as illustrated in Fig. 6(b). The measured detection limit of anti-IgG was 2.5 ng/mL, or 16.7 pM [28].

We have also extended the phase-interrogation method to the integrated resonance-based sensor chip [26]. An all-pass SOI ring resonator is adopted as the sensing element. Figure 7(a) shows a picture of a fabricated SOI ring with a diameter of 40 μm, together with a coupling bus waveguide. A simple microfluidic channel is attached on top of the ring for delivering the analytes, as shown in Fig. 7(b). In order to measure the phase, two laser beams at slightly different wavelengths are launched simultaneously in the bus waveguide. One is located close to the resonance, and the other is located away from it,

Table 2: Performance comparison of some SERS structures. NP: nanoparticle; SS: solid substrate; 4-MBT: 4-methyl benzenthiol; 2-Mpy: 2-methyl pridine; N.A.: not described in the paper.

Substrate	Metal	Characteristic dimension	EF	Molecule	Fabrication method
NP dimer [77]	Ag	1.8 nm	2×10^7	4-MBT	Polyol process
NP shell [78]	Au/SiO_2	2–20 nm	4×10^8	N.A.	Sol-gel process
NP aggregation [42]	Ag	N.A.	10^{14} –10^{15}	R6G	Silver colloid solution
NP gap [79]	Au	1 nm	1.0×10^8 –5.0×10^9	DNA spacer	DNA modified Au nanogap
NP nanostar [80]	Au	N.A.	5×10^5	2-Mpy	Seed-mediated growth
SS INPG [44]	Au	N.A.	10^7	BT	LIL, edge lithography, and anisotropic etching
SS Nano gap [32]	Au	5 nm	10^9	BT	Photolithography, metal layer sacrificing
SS Nano gratings [81]	Au	8.5 nm	10^6	Thioninacetate	Holographic lithography, Au layer deposition
SS Nano slit [45]	Au	10 nm	10^7	BT	E-beam lithography, Au layer deposition

as indicated by the dash-dotted lines in Fig. 2. A single-sideband generation technology can be used to generate such beams. When the resonant wavelength is shifted by the incorporation of the analyte, the imposed phase on the on-resonance laser will change rapidly, while that on the off-resonance laser will almost stay constant. In other words, the on-resonance and off-resonance lasers can be used as the sensing and the reference beams, respectively. The phase induced by the ring can be extracted through methods such as measuring the interference between these two laser beams using a coherent detection technology. It is worthwhile to note that a high-Q resonator is preferred in this case. As denoted in Fig. 2(b), a high-Q resonator will provide a steeper phase transition around the resonance, and the sensing and the reference laser beams can be placed closer to each other, which makes the generation and detection of them easier. We refer to Refs. [26] & [76] for the detailed discussions about the measurement techniques.

To test the phase interrogation technology, aqueous NaCl solutions of various concentrations were used as the analytes, which were injected sequentially on top of the SOI ring through the microfluidic channel. The measured phase response of the ring is plotted in Fig. 8(a), which matches well with the theoretical prediction using the parameters of the ring derived from the measured power transmission response. A maximal sensitivity of the present sensing device reaches 6×10^3 rad/RIU. To further investigate the stability of the sensing response, a kinetic measurement was also performed as shown in Fig. 8(b). Due to the adopted phase interrogation technology and the shared light path between the sensing and the reference beams, most of the intensity noises were shielded. When the analyte concentration became stable, a stable phase reading with a typical 3σ noise of 0.015 rad can be obtained. Taking into account the maximal sensitivity of 6×10^3 rad/RIU discussed above, the detection limit of the phase-interrogation approach reached 2.5×10^{-6} RIU.

3 SERS-based sensing substrates with metallic nanostructures

3.1 Large-area SERS substrates

In the past 40 years, numerous SERS substrates were developed and applied in abroad research fields. Table 2 lists the characteristic dimensions and SERS EF performance of some SERS substrates. The table also includes the fabrication method, the type of metal, SERS EF, and SERS characterization molecule used for testing the structures. Among them, metallic nanoparticals (MNPs) attracted much attention for its high SERS-performance and ease of synthesis. Coinage MNPs, such as Au, Ag, were synthesized with different sizes, shapes, and applied in biological analy-

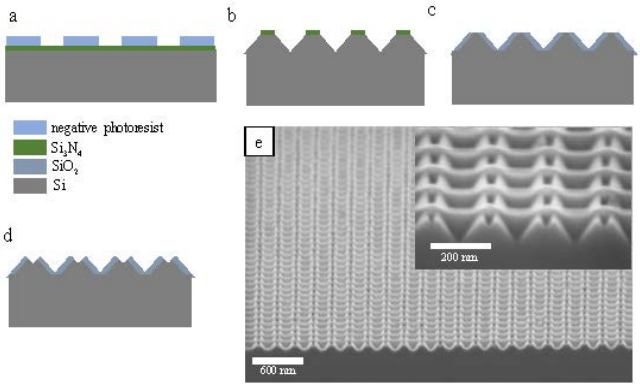

Figure 9: Fabrication overview of the INPG structure. (a) Nanopatterning by LIL. (b) After dry etching of the SiN mask and KOH wet anisotropic etching. (c) After thermal oxidation and removing the SiN mask by hot H_3PO_4. (d) INPGs were fabricated by the second KOH wet etching. (e) Picture of a fabicated INPG structure. Adapted from Ref. [44].

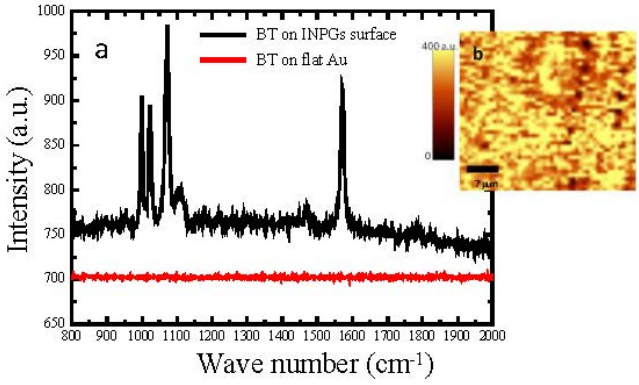

Figure 10: SERS measurement results. (a) Monolayer BT Raman spectra measured from the Au coated INPG surface (black) and a flat Au surface (red); (b) 1600 μm^2 Raman mapping on the Au coated INPG surface. Raman shift spectra at 990 cm^{-1} was used to make the Raman map. Adapted from Ref. [44].

sis, chemical identification, and material area [42, 77–80]. However, the application of such a SERS chip is largely limited by the aggregation and low reproducibility including the intensity spatial variations and sample-to-sample variations. Tian's group made a progress to avoid aggregation [78], where they proposed a kind of shell isolated MNPs as smart SERS enhancing dust to keep the particles from agglomerating. In an early work by Freeman et al. [82], MNPs immobilized on glass slides could reach a spatial variation of 5% to 8% in SERS efficiency. In the last decade, as the fast development of nanofabrication techniques such as electron beam lithography (EBL), nanostructrues with details below 10 nm could be fabricated successfully. These top-down methods soon became powerful tools in the study of SERS, because it allows researchers to fabricate complex metallic nanostructures with predesigned profiles with perfect position, which do not suffering from the aggregation and low reproducibility. It still gives us unprecedented opportunities to look much deeper into the essence of SERS. Many different kinds of ordered nanostructures have been carried out to improve the electric field enhancement at the position of hot-spot (and eventually the SERS effect) [33, 44–46, 81].

Utilizing the well-known anisotropic wet-etching of silicon, inverted pyramidal structures in micron- or nanoscale can be conveniently fabricated on the (100) single crystal silicon wafer. This type of inverted pyramidal structures have been studied intensively, and have been used for SERS for decades. For example, the most successfully commercialized SERS substrate, called Klarite® [83], consists of micron-scale inverted pyramidal structures. In order to further increase the SERS efficiency, we have fabricated nanoscale pyramidal structures with high density using EBL technology [34, 84]. A great SERS EF was obtained. However, the conventional fabrication method for inverted pyramidal structures results in a flat boundary area between the two adjacent inverted pyramids, which decreases the homogeneity of the SERS enhancement distribution on the substrate surface, since a flat metallic surface can only contribute slightly on enhancing the Raman signal. The EBL process is also not cost-effective for large-area substrates. Recently, we introduced an INPG structure on a single crystal silicon wafer in a large scale (100 μm × 100 μm) combining laser interference lithography (LIL), edge lithography, and anisotropic etching technologies, where the flat area can be effectively removed by introducing a nanogroove on it. The whole process starts with the conventional fabrication of the inverted nanopyramids as shown in Fig. 9 [44]. After the first step of wet anisotropic etching, the substrate underwent a thermal oxidation process where the pyramidal walls were oxidized with a proper thickness. Then the mask material was removed, and the flat surface between the two neighboring pyramidal holes was exposed. The substrate was immediately immersed in hot KOH for the second wet etching to form the nanogrooves. Figure 9(e) shows a fabricated INPG structure. In the final step, an Au film of 50 nm was deposited on the substrate. The Raman measurement was applied using benzenethiol (BT) as a characterization molecule. BT is a widely used SERS characterization molecule since it has a relatively large Raman cross section and a limited number of well-studied Raman active vibrational modes. In addition, it does not fluoresce in the visible spectrum. The breathing vibrational mode of the benzene ring at 990 cm^{-1} was used for Raman signal mapping on the substrate in order to evaluate the Raman signal ho-

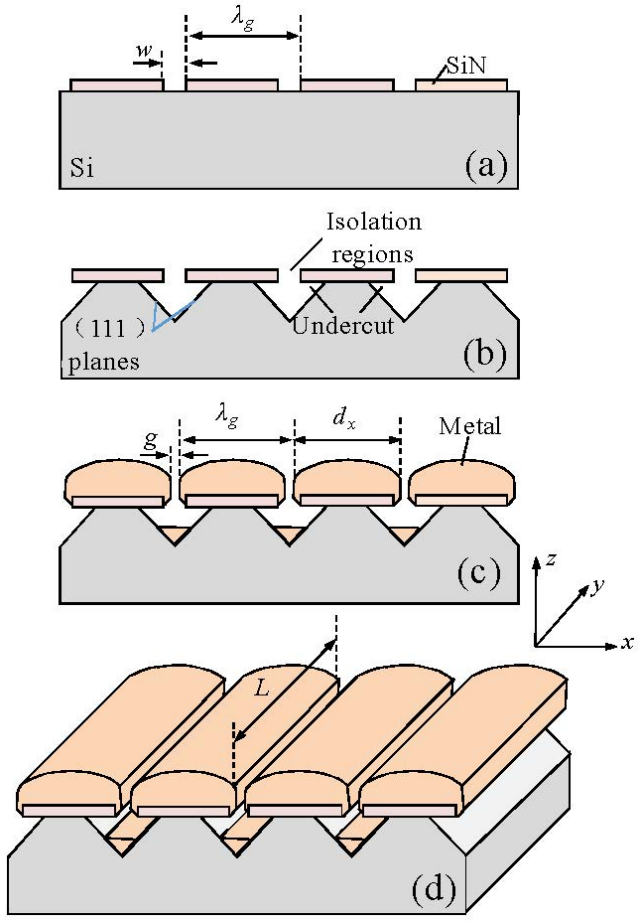

Figure 11: Top-down metallic nanowire array fabrication procedure and relevant dimensions (not to scale). (a) SiN mask layer with the length direction aligned to the [110] direction of a (100) silicon wafer. (b) Anisotropic etching of silicon to create the triangular undercut grooves. (c) Metal deposition using conventional vacuum deposition technology. (d) Finished metallic nanowire array. Adapted from Ref. [45].

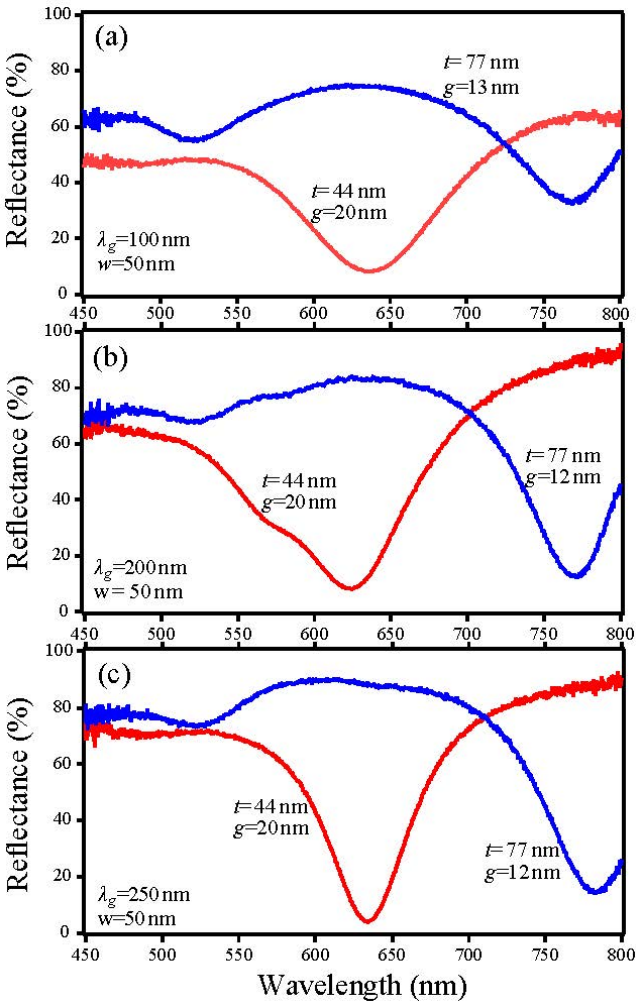

Figure 12: Measured reflectance of Au nanowires array surfaces with different pitches λ_g and nanogap widths g, using an incident light polarization perpendicular to the nanowires. Adapted from Ref. [45].

mogeneity of the SERS substrate. As shown in Fig. 10(a), one can find that the Raman signal of the BT molecule was dramatically enhanced on the fabricated INPG structure compared to that on a flat substrate. The calculated EF is 10^7. The Raman mapping result shown in Fig. 10(b) demonstrates that the distribution of the SERS "hot spot" is homogeneous on the proposed substrate.

Nanogap between metals is known as one of the best SERS structure since the coupled surface plasmon mode can be generated between the gaps if the gap distance is in the order of nanometers. As a result the Raman signal can be dramatically enhanced [22]. Scientists nowadays focused on how to fabricate this type of narrow nanogaps in a large-area SERS substrate. In 2005, Hui Wang et al., through casting the nanoparticles on a flat surface, formed high density adjacent nanogaps (less than 10 nm). The SERS EF greater than 10^8 was achieved on such a substrate [85]. However, there were still many defects on the substrate since the nanoparticles were self-assembly patterned. In 2010, Deng et al. used the holographic technology as the pattering technology [81]. By controlling the Au layer deposition, the nanogap between two nanogratings is well controlled with a width of 8.5 nm and a period of 350 nm, which provided a uniform SERS EF. It is also revealed that the polarization of the incident light will dramatically influence the SERS signal. Im et al. combined the photolithography with scarifying layer technology to fabricate a large-area SERS substrate with 7-nm nanogaps [32]. The SERS EF is in the order of 10^9.

We employed a top-down process combining EBL, silicon anisotropic wet etching, and thin metallic film deposition technologies to fabricate high density metallic nanowire arrays with a well controllable wire-to-wire dis-

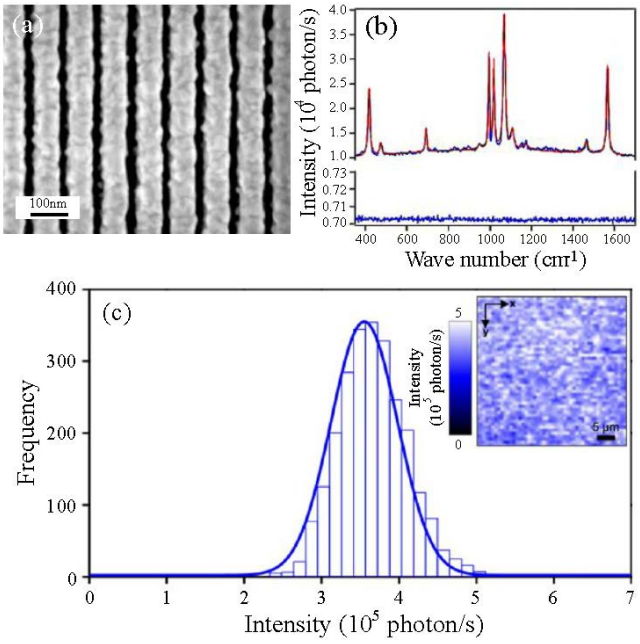

Figure 13: (a) Image of the Au nanowire array surface. (b) Measured SERS spectra of BT chemisorbed on a Au nanowire array (top) and flat-Au surfaces (bottom). The red curve indicates the fitted Lorentzian bands. (c) Histogram of 1068 cm^{-1} band integrated intensity from the Raman mapping over a 40 × 40μm^2 area (inset) and fitted Gaussian distribution. Adapted from Ref. [45].

tance, that is, the gaps, which are beneficial to obtain a uniform SERS efficiency [45]. The detailed processing is illustrated in Fig. 11. First, triangular undercut grooves were fabricated on a (100) single crystal silicon substrate using similar fabrication steps for inverted pyramids as discussed in the previous section. The metallic nanowire array was subsequently realized, using vacuum deposition technology, on the surface of the SiN mask used for the wet etching. By controlling the thickness of the deposited metallic layer, the nanogap between the two nanowires can be well tuned and less than the feature size, down to 10 nm.

The enhanced optical field results from the coupled surface plasmon mode between two metallic nanowires can be optically characterized by using light absorption measurements. As shown in Fig. 12, the reflectance minimum λ_L (which is an indication of the excitation wavelength of the coupled surface plasmon mode) of the Au nanowire arrays with different periods λ_g of the wires and gaps g can be precisely tuned from 633 to 785 nm, where most of the Raman excitation laser sources reside (e.g. 532, 633, and 785 nm). In all cases, λ_L red-shifts when g is decreased, which demonstrates a strong dependence of the couple-mode localized SPR on the nanogaps. A monolayer of BT molecules was self-assembled on the fabricated Au nanowire arrays shown in Fig. 13(a), and was applied for characterizing the SERS properties. The Raman signals from the substrate show clear BT fingerprint vibrational modes at, for example, 416, 691, 994, 1018, 1068, and 1565 cm^{-1} as illustrated in Fig. 13(b). The uniformity of the SERS effect was mapped using the 1068 cm^{-1} vibration mode, and the histogram of the integrated intensity is given in Fig. 13(c). One can find that the measured SERS effect is highly homogeneous on the Au nanowire arrays with only an 11% variation over the measured surface. The SERS EF G_{AEF} can be calculated using the standard formula, $G_{AEF} = (I_{SERS}/N_{SERS})(I_{RS}/N_{RS})^{-1}$, where I_{SERS} and I_{RS} are the integrated intensities from the SERS substrate and a conventional Raman substrate with a flat Au surface, respectively, and N_{SERS} and N_{RS} are the number of molecules in the collection volumes on the two substrates, respectively. After analyzing 3000 Raman spectra from BT monolayer molecules, $G_{AEF} \approx 1.2 \times 10^7$ can be calculated on the fabricated Au nanowire array surface. The above results show that a very controllable, uniform, and great SERS efficient substrate is provided with a high density and a large number of hot spots.

3.2 SERS substrates with double resonance structures

In the previous sections, typical plasmonic resonances among those nanostructures can provide efficient enhancements for the SERS process. Most of these enhancements work well for small wave-number Raman signals, that is, the Raman shift is small and the plasmonic resonance could cover both the excitation light and the Raman scattering signal. However, for larger wave-number Raman processes, the width of a common (single) plasmonic resonance is too narrow to cover both the excitation and scattered signals, which will hinder the performance of the SERS substrates. For example, the stokes line of C-H vibration is near 3000 cm^{-1}, while the typical resonance of a plasmonic structure could only cover the wave-number range below 1000 cm^{-1}.

To address the Raman enhancement at long wavenumbers, dual-resonance plasmonic SERS chip is proposed recently and quickly attracts much interest. Chu et al. demonstrated a multilayer structure that supports both the nonlocal surface propagating plasmon resonance and localized SPR modes [86]. By utilizing the hybridization between these two modes, dual enhancement peaks appear to provide enhancement to the excitation wavelength and the scattering wavelength simultaneously. However, the limited tunability of the two enhancement peaks

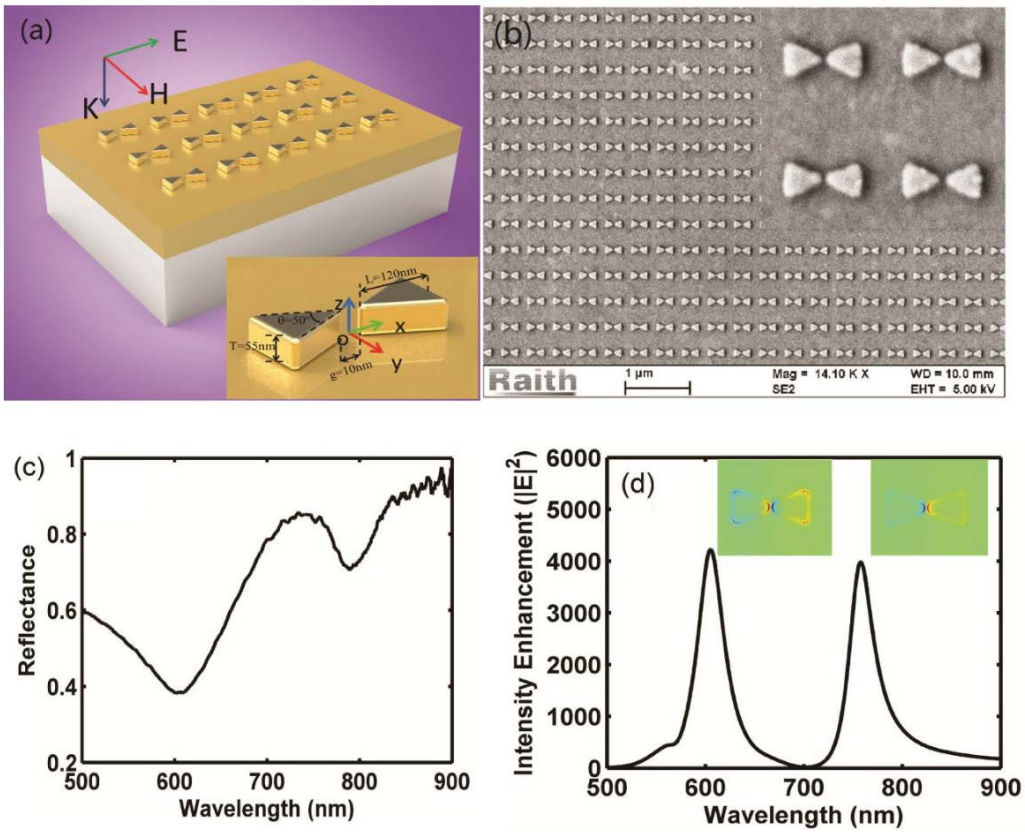

Figure 14: (a) Schematic of the dual-resonance Au device. (b) Picture of the fabricated nano-bowtie array on an opaque Au film. (c) Measured reflection spectrum for the nano-bowtie array. (d) Intensity enhancement spectrum obtained at the middle point of the gap with E_z profiles of the two resonances on the top surface of the bowtie structure. The structure parameters are indicated in (a) with an array period of 560 nm. Adapted from Ref. [46].

by mode hybridization greatly hindered its applications. Later, another kind of dual-resonance structure consisting of a pair of mixed dimer was introduced [87]. Two types of dimer were fabricated alternatively on the substrate, each type of dimer dominates one distinct plasmonic resonance, therefore the resonance position could be controlled separately by changing the parameters of corresponding dimer. The mixed dimer substrate supports two localized SPR modes, but the hot-spots of the two modes are not exactly matched, which would decrease the Raman efficiency. To improve the performance of dual-resonance SERS substrate, we designed and fabricated an Au nano-bowtie array directly on a uniform and optically opaque Au film as shown in Fig. 14(a) and 14(b), which provides high independent tunability and spatially well-matched hot-spots for the two resonances [46]. A plane wave impinging on the chip with the electric field polarized along the bowtie axis would excite both the electric dipole binding resonance (EDBR) and the out of plane magnetic dipole resonance (MR). Correspondingly, two obvious dips in reflection spectrum could be detected (cf., Fig. 14(c)) and strong field enhancement at both resonances can be observed (cf., Fig. 14(d)). Superior to other dual-resonance structures [86, 87], which utilize the coupling between nonlocal surface propagating plasmon resonance and localized SPR modes, the tunability of the resonance positions of the proposed structure has more freedom. We find that EDBR and MR can be tuned by the arm length and thickness of the bowtie, respectively. In addition, another advantage of our structure is the spatial overlap of the "hot spot" of both resonances, which is essential to the simultaneous enhancement of excitation and specific scattering lines. Three samples with different parameters were fabricated, and a poly-methyl-methacrylate (PMMA) layer is cladded over each sample, from which Raman signals were collected by a commercial Renishaw system to compare their performance. Here, the excitation wavelength is at 785 nm and the specific Raman signal under investigation is at 2960 cm^{-1} (which is one characteristic vibration line of PMMA), as indicated by the dashed purple and cyan lines, respectively, in Fig. 15(a). One can see that, in Fig. 15(a), sample B, which corresponds to the red curve,

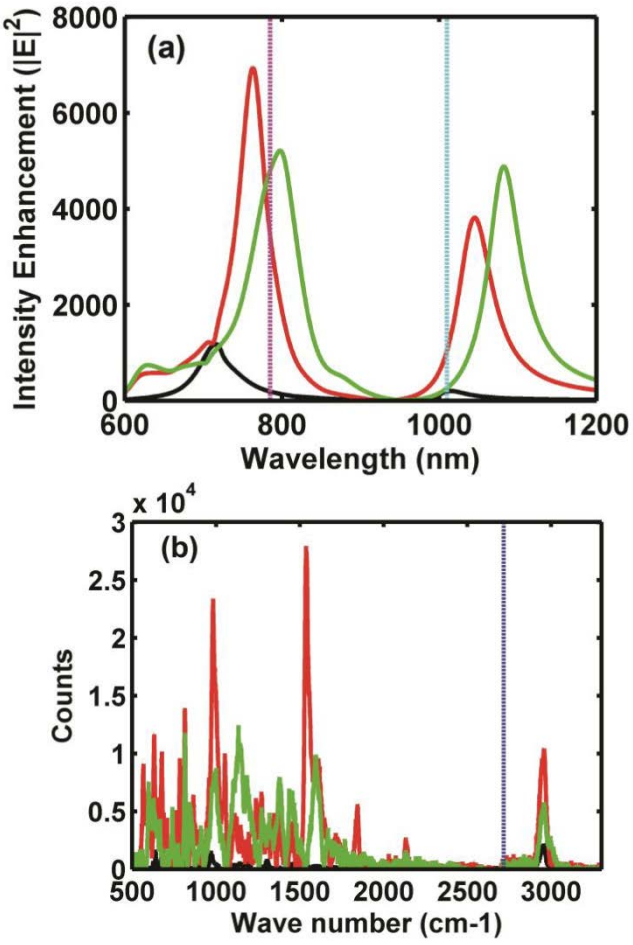

Figure 15: (a) Simulated intensity enhancement spectra. The dashed violet line marks the wavelength of the pump laser and the dashed cyan linemarks the position of the Raman signal at 2960 cm^{-1}. (b) Measured Raman spectra of PMMA for the three structures in our experiment. The Raman signal with a wave number larger than the blue line position is magnified by four times for clarity. The black, red, and green spectra in (a) and (b) respectively correspond to structure A: L =100 nm, g =25 nm, T =60 nm, θ =50°; structure B: L =120nm, g =10 nm, T =55 nm, θ =50°; and structure C: L =140 nm, g =10 nm, T =60 nm, θ =50°. Adapted from Ref. [46].

provides the best match between the two resonant peaks and the two lines indicating the excitation and Raman scattering wavelengths. As a result, in Fig. 15(b), the corresponding measured scattering curve (red) exhibits the strongest Raman signal intensity at 2960 cm^{-1}.

4 Conclusions and Perspectives

We have introduced some silicon and metallic nanostructures as well as integrated chips including evanescent-wave-based refractive index sensing chips and SERS chips. On the growing requirement from the biological and agricultural societies, the optical technologies discussed in this review have been largely pushed toward practical and commercial label-free sensors in the recent years. Prism or grating coupled SPR sensors are probably the most successfully commercialized one, and have been studied to realize label-free interaction analysis in real-time. Biacore systems are the most widely used and excellent SPR sensors, which can characterize molecules in terms of specificity of their interactions, on and off rates (kinetics), and binding strength (affinity). Biacore can also provide sensitive and accurate concentration measurements. All the data from an interaction can be visualized from Biacore sensorgrams. Drug discovery and development, biotherapeutics, and life science research can be carried out based on this system. Rich et al. used Biacore 2000 and Biacore 3000 optical biosensors equipped with research-grade CM5 sensor chip to measure drug/human serum albumin (HSA) interactions with high resolution [88]. However, Biacore system is an expensive platform. The SensiQ Pioneer ST breaks new ground and makes label-free SPR analysis accessible for any academic laboratory. SensiQ can provide high-data quality and exceptional performance for studying protein interaction kinetics, characterizing antibodies, and screening small molecules drug candidates. The SPR sensor for laboratory use are usually bulky and not suitable for field application. Spreeta sensors are one of examples of miniaturized SPR sensors. Particularly, the sensor module TSPR1K23 containing three channels which enables parallel detection. Hu et al. designed and validated a low cost and delicate SPR biosensor based on three-channel Spreeta TSPR1K23 to monitor the interaction between the hepatitis B surface antigen and the hepatitis B surface antibody [89]. Nowadays, most of commercialized SPR sensors are based on intensity or angular interrogation SPR because of simple optical platforms and brief software programs. However, few phase-sensitive SPR systems can be founded in market mainly due to two difficulties: First, a stable and low-cost phase modulator have to be added into the optical platform. Second, phase-sensitive SPR sensor produces a very high sensitivity but companied with low dynamic range which limits to biological and chemical applications. In the future, methods to widen the dynamic range should be further developed for the phase-sensitive SPR system. Concerning integrated sensor chips based on SOI, although the technology is relatively new, Genalyte recently made a great progress in commercializing the Maverick Detection System [90]. Each consumable chip used by this instrument contains 1-128 sensor elements (including 8 for controls) made of SOI ring resonators. This system can directly de-

tect hybridizing DNA in tens of pM, which is about 10 times better than what a standard ELISA test can give.

On the other hand, as Raman signal is the information about molecular vibration, SERS is well recognized as a fingerprint technology for identifying the molecules. For bioapplications, SERS was mainly applied as identification technology like bacteria identification, intracellular signal tracking tag, label-free cell imaging. At an early stage, SERS was just applied on the bacteria surface for identifying the bacteria with different Raman signal. It is difficult to study the bacterium in quantity since all Raman spectra only reveal the vibration information about the molecules at the substrate surface [91]. Cowcher David et al. developed a nanoparticle-based SERS system to detect the bacteria expressed small molecule for the bacteria identification [92]. By incubating the cells with nanoparticles, the nanoparticles will diffuse into the cell and accumulate in the lysosomes [93]. However, not like nanoparticle systems, the solid-based SERS substrate could not get into the cell as free as nanoparticles. In most applications, the solid-based SERS was focused the organic molecule [32, 44, 45, 81] and bacteria identification [94–97]. Yamazoe et al. first applied a gold nanocoral structure which is solid-based transparent boehmite for visualizing the ischemic core of mouse brain without labeling and pretreatment of the tissue [98]. This work opened a new window for label-free tissue imaging using large scale solid base SERS substrate.

Recent progress in nanofabrication and integration technologies enables the development of highly sensitive, multifunctional, and stable platforms for optical label-free sensing. Although many challenges exist, the lab-on-a-chip system integrating the discussed refractive index and SERS sensing technologies together with optical signal generation, spectroscopes, optical detection, and microfluidics would be an important direction of research to pursue in the near future. Because of the joint and multidiscipline efforts from optics, chemical, and biology, as well as research institutes and industries, we could expect that portable, cheap, standard, and easy-to-handle optical label-free biosensing devices employing lab-on-a-chip systems would play important roles in future health care, food safety, and environment monitoring.

Acknowledgement: This research is partially supported by "863" project (Ministry of Science and Technology of China, #2012AA012201), National Nature Science Foundation of China (#61107020, #61377023, and #61108022), and the Guangdong Innovative Research Team Program (#201001D0104799318).

References

[1] R. Narayanaswamy, O.S. Wolfbeis, Optical Sensors, Springer, New York, 2004.
[2] M. A. Cooper, Optical biosensors in drug discovery. Nature Reviews Drug Discovery, 1(7):515–528, 2002.
[3] P. Yager, T. Edwards, E. Fu, K. Helton, K. Nelson, M. R. Tam, and B. H. Weigl, Microfluidic diagnostic technologies for global public health. Nature, 442(7101):412–418, 2006.
[4] K. R. Rogers, Recent advances in biosensor techniques for environmental monitoring. Analytica Chimica Acta, 568(1-2):222–231, 2006.
[5] L.M. Lechuga, in: Biosensors and Modern Biospecific Analytical Techniques, Vol. 44, edited by L. Gorton (Elsevier Science BV, Amsterdam, Netherlands, 2005).
[6] W.E. Moerner, New directions in single-molecule imaging and analysis. Proceedings of the National Academy of Sciences of the United States of America, 104(31):12596–12602, 2007.
[7] R.M. Lequin, Enzyme Immunoassay (EIA)/Enzyme-Linked Immunosorbent Assay (ELISA). Clinical Chemistry, 51(12):2415–2418, December 2005.
[8] X. Fan, I.M. White, S.I. Shopova, H. Zhu, J.D. Suter, and Y. Sun, "Sensitive optical biosensors for unlabeled targets: A review", Anal. Chim. Acta 620, 8-26 (2008).
[9] W.G. Cox, V.L. Singer, Biotechniques 36 (2004) 114.
[10] U.B. Nielsen and B.H. Geierstanger. Multiplexed sandwich assays in microarray format. Journal of Immunological Methods, 290(1-2):107– 120, July 2004.
[11] M.L. Phelan and S. Nock. Generation of bioreagents for protein chips. Proteomics, 3(11):2123–2134, November 2003.
[12] Martin Nirschl, Florian Reuter, and Janos Vörös, Review of Transducer Principles for Label-Free Biomolecular Interaction Analysis. Biosensors, 1(3):70–92, 2011.
[13] M.-Carmen Estevez, Mar Alvarez and Laura M. Lechuga, "Integrated optical devices for lab-on-a-chip biosensing applications", Laser Photonics Rev. 6, No. 4, 463–487 (2012).
[14] Abraham J. Qavi, Adam L. Washburn, Ji-Yeon Byeon, and Ryan C. Bailey, Label-free technologies for quantitative multiparameter biological analysis. Anal. Bioanal. Chem., 394(1):121–135, May 2009.
[15] K. Kneipp, M. Moskovits, H. Kneipp, Surface-Enhanced Raman Scattering: Physics and Applications, Springer, Berlin, Germany, 2006.
[16] S. Schlucker, Surface Enhanced Raman Spectroscopy: Analytical, Biophysical and Life Science Applications, Wiley-VCH, Weinheim, Germany, 2011.
[17] B.E.A. Saleh and M.C. Teich, Fundamentals of Photonics. John Wiley and Sons, Inc, Hoboken, New Jersey, 2007.
[18] W. Lukosz, Integrated optical chemical and direct biochemical sensors. Sensors and Actuators B -Chemical, 29:37–50, 1995.
[19] Jeffrey J. Lillie, Mikkel A. Thomas, Nan-Marie Jokerst, Stephen E. Ralph, Karla A. Dennis, and Clifford L. Henderson, "Multimode interferometric sensors on silicon optimized for fully integrated complementary-metal-oxide-semiconductor chemical-biological sensor systems", J. Opt. Soc. Am. B 23, 642-651 (2006).
[20] Katrin Schmitt, Bernd Schirmer, Christian Hoffmann, Albrecht Brandenburg, Patrick Meyrueis, "Interferometric biosensor based on planar optical waveguide sensor chips for label-free

detection of surface bound bioreactions", Biosensors & Bioelectronics, 22(11), 2591-2597, 2007

[21] X.D. Hoa, A.G. Kirk, and M. Tabrizian, Towards integrated and sensitive surface plasmon resonance biosensors: A review of recent progress. Biosensors & Bioelectronics, 23(2):151–160, 2007.

[22] H. Raether, Surface Plasmons (Springer, Berlin, 1988).

[23] W. Bogaerts, R. Baets, P. Dumon, V. Wiaux, S. Beckx, D. Taillaert, B. Luyssaert, J. Van Campenhout, P. Bienstman, and D. Van Thourhout. Nanophotonic waveguides in silicon-on-insulator fabricated with CMOS technology. Journal of Lightwave Technology, 23(1):401–412, 2005.

[24] K Yao and Y. Shi, eHigh-Q width modulated photonic crystal stack mode-gap cavity and its application to refractive index sensinge, Opt. Express 20(24), 27039-+27044 (2012).

[25] P. Xu, K. Yao, J. Zheng, X. Guan, and Y. Shi, "Slotted photonic crystal nanobeam cavity with parabolic modulated width stack for refractive index sensing", Optics Express 21(22): 26908–26913 (2013).

[26] J. Liu, X. Zhou, Z. Qiao, J. Zhang, C. Zhang, T. Xiang, L. Shui, Y. Shi, L. Liu, "Integrated Optical Chemical Sensor Based on an SOI Ring Resonator Using Phase-Interrogation", IEEE Photonics Journal 6, 6802207 (2014).

[27] G. Ye, W. Yang, L. Jiang, S. He, Surface plasmon resonance phase-sensitive imaging (SPR-PI) sensor based on a novel prism phase modulator. PIER 2014; 145:309–9.

[28] G. Ye, W. Yang, L. Jiang, J. Qian, S. He, A novel phase-sensitive SPR biosensor array based on prism phase modulator. Proc. of SPIE 2014; 8989.

[29] M. Fleischm, P.J. Hendra and Mcquilla Aj, "Raman-Spectra of Pyridine Adsorbed at a Silver Electrode", Chem Phys Lett 26(2), 163-166 (1974).

[30] D.K. Lim et al., "Nanogap-engineerable Raman-active nanodumbbells for single-molecule detection", Nat Mater 9(1), 60-67 (2010).

[31] L.M. Tong, H.X. Xu, and M. Kall, "Nanogaps for SERS applications", Mrs Bull 39(2), 163-168 (2014).

[32] H. Im et al., "Vertically Oriented Sub-10-nm Plasmonic Nanogap Arrays", Nano Lett 10(6), 2231-2236 (2010).

[33] G. Lu et al., "High-density metallic nanogaps fabricated on solid substrates used for surface enhanced Raman scattering", Nanoscale 4(3), 860–863 (2012).

[34] M.L. Jin et al., "High-Density Periodic Arrays of Self-Aligned Subwavelength Nanopyramids for Surface-Enhanced Raman Spectroscopy", J Phys Chem C 114(50), 21953–21959 (2010).

[35] S.Y. Lin et al., "Surface-Enhanced Raman Scattering with Ag Nanoparticles Optically Trapped by a Photonic Crystal Cavity", Nano Lett 13(2), 559–563 (2013).

[36] C.C. Ho, K. Zhao, and T.Y. Lee, "Quasi-3D gold nanoring cavity arrays with high-density hot-spots for SERS applications via nanosphere Lithography", Nanoscale 6(15), 8606–8611 (2014).

[37] C. Chen et al., "Focusing Plasmons in Nanoslits for Surface-Enhanced Raman Scattering", Small 5(24), 2876–2882 (2009).

[38] C. Chen et al., "Raman scattered photon transmission through a single nanoslit", Appl Phys Lett 96(6), (2010).

[39] M.A. Seo et al., "Terahertz field enhancement by a metallic nano slit operating beyond the skin-depth limit", Nat Photonics 3(3), 152–156 (2009).

[40] S.K. Ghosh, and T. Pal, "Interparticle coupling effect on the surface plasmon resonance of gold nanoparticles: From theory to applications", Chem Rev 107(11), 4797–4862 (2007).

[41] S.M. Stranahan, and K.A. Willets, "Super-resolution Optical Imaging of Single-Molecule SERS Hot Spots", Nano Lett 10(9), 3777–3784 (2010).

[42] Dana Cialla, Sibyll Pollok, Carolin Steinbrücker, Karina Weber, and Jürgen Popp, "SERS-based detection of biomolecules", Nanophotonics. Volume 3, Issue 6, Pages 383–411, October 2013

[43] S.M. Nie, and S.R. Emery, "Probing single molecules and single nanoparticles by surface-enhanced Raman scattering", Science 275(5303), 1102–1106 (1997).

[44] M. Jin et al., "An Inverted Nano Pyramids and Grooves Surface for Surface Enhanced Raman Spectroscopy", Journal of Nanoengineering and Nanomanufacturing 4(294–298 (2014).

[45] L.L.T. Ngoc et al., "Large Area Metal Nanowire Arrays with Tunable Sub-20 nm Nanogaps", Acs Nano 7(6), 5223–5234 (2013).

[46] Jiao Lin, Yuan Zhang, Jun Qian and Sailing He, A nano-plasmonic chip for simultaneous sensing with dual-resonance surface-enhanced Raman scattering and localized surface plasmon resonance. Laser & Photonics Review 2014; 8: 610–6.

[47] J. Homola, Surface plasmon resonance sensors for detection of chemical and biological species. Chem. Rev 2008; 108: 462–31.

[48] E. Ouellet, C. Lausted, T. Lin, C.W.T. Yang, L. Hood, E. Lagally, Parallel microfluidic surface plasmon resonance imaging arrays. Lab Chip 2010; 10: 581–7.

[49] Y. Luo, F. Yu, R. Zare, Microfluidic device for immunoassays based on surface plasmon resonance imaging. Lab Chip 2008; 8: 694–6.

[50] M. Piliarik, H. Vaisocherova, J. Homola, "Towards parallelized surface plasmon resonance sensor platform for sensitive detection of oligonucleotides", Sensors and Actuators B 121, 187–193 (2007)

[51] B. Sepulveda, A. Calle, L.M. Lechuga, G. Armelles, "Highly sensitive detection of biomolecules with the magneto-optic surface-plasmon-resonance sensor", Optics Letters 31(8), 1085–1087 (2006)

[52] H. Pedersen, C. Thirstrup, "Design of near-field holographic optical elements by grating matching", Applied Optics 43(6), 1209–1215 (2004).

[53] G. Nenninger, M. Piliarik, J. Homola, "Data analysis for optical sensors based on spectroscopy of surface plasmons", Measurement Science and Technology 13, 2038–2046 (2002)

[54] R. Slavik, J. Homola, "Ultrahigh resolution long range surface plasmon-based sensor", Sensor and Actuators B123, 10–12 (2007).

[55] I.M. White and X. Fan, "On the performance quantification of resonant refractive index sensors", Opt. Express 16, 1020–1028 (2008).

[56] K. De Vos, I. Bartolozzi, E. Schacht, P. Bienstman, and R. Baets, "Silicon-on-insulator microring resonator for sensitive and label-free biosensing", Opt. Express, vol. 15, no. 12, pp. 7610–7615, Jun. 2007.

[57] Tom Claes, Wim Bogaerts, and Peter Bienstman, "Experimental characterization of a silicon photonic biosensor consisting of two cascaded ring resonators based on the Vernier-effect and introduction of a curve fitting method for an improved detection limit", Opt. Express 18, 22747–22761 (2010)

[58] D.K. Armani, T.J. Kippenberg, S.M. Spillane and K.J. Vahala, "Ultra-high-Q toroid microcavity on a chip", Nature, vol. 421, pp. 925–929, 2003.

[59] Andrea M. Armani, Rajan P. Kulkarni, Scott E. Fraser, Richard C. Flagan, and Kerry J. Vahala, "Label-Free, Single-Molecule Detection with Optical Microcavities", Science 317, 783–787, 2007.
[60] M. Iqbal et al., "Label-free biosensor arrays based on silicon ring resonators and high-speed optical scanning instrumentation", IEEE J. Sel. Topics Quantum Electron., vol. 16, no. 3, pp. 654–661, May 2010.
[61] D.-X. Xu et al., "Label-free biosensor array based on silicon-on-insulator ring resonators addressed using a WDM approach", Opt. Lett., vol. 35, no. 16, pp. 2771–2773, Aug. 2010.
[62] M. Notomi, "Manipulating light with strongly modulated photonic crystals", Reports on Progress in Physics, 73, 096501, pp. 57, (2010).
[63] P.B. Deotare, M.W. McCutcheon, I.W. Frank, M. Khan, and M. Lončar, "High quality factor photonic crystal nanobeam cavities", Appl. Phys. Lett. 94(12), 121106 (2009).
[64] M. Notomi, E. Kuramochi, and H. Taniyama, "Ultrahigh-Q Nanocavity with 1D Photonic Gap", Opt. Express 16(15), 11095–11102 (2008).
[65] S. Mandal, X. Serey, and D. Erickson, "Nanomanipulation using silicon photonic crystal resonators", Nano Lett. 10(1), 99–104 (2010).
[66] Sudeep Mandal and David Erickson, "Nanoscale optofluidic sensor arrays", Opt. Express 16, 1623–1631 (2008).
[67] V.R. Almeida, Q. Xu, C.A. Barrios, and M. Lipson, "Guiding and confining light in void nanostructures", Opt. Lett., vol. 29, no. 11, pp. 1209–1211, Jun. 2004.
[68] T. Claes, J.G. Molera, K. De Vos, E. Schacht, R. Baets, and P. Bienstman, "Label-free biosensing with a slot-waveguide-based ring resonator in silicon on insulator", IEEE Photonics J.1(3), 197–204 (2009).
[69] A. Di Falco, L. O'Faolain, and T. F. Krauss, "Chemical sensing in slotted photonic crystal heterostructure cavities", Appl. Phys. Lett. 94(6), 063503 (2009).
[70] Joyce Poon, Jacob Scheuer, Shayan Mookherjea, George Paloczi, Yanyi Huang, and Amnon Yariv, "Matrix analysis of microring coupled-resonator optical waveguides", Opt. Express 12, 90–103 (2004).
[71] C. Wu, Z. Jian, S. Joe, L. Chang, "High-sensitivity sensor based on surface plasmon resonance and heterodyne interferometry", Sensors and Actuactors B 92, 133–136 (2003)
[72] W. Yuan, H. Ho, S. Wu, Y. Suen, S. Kong, "Polarization-sensitive surface plasmon enhanced ellipsometry biosensor using the photoelastic modulation technique", Sensors and Actuators A 151, 23–28 (2009)
[73] Y. Shao, Y. Li, D. Gu, K. Zhang et al. "Wavelength-multiplexing phase-sensitive surface plasmon imaging sensor", Optics Letters 38(9), 1370–1372 (2013).
[74] S. Wu, H. Ho, W. Law, C. Lin, "Highly sensitive differential phase-sensitive surface plasmon resonance biosensor based on the Mach-Zehnder configuration", Optics Letters 29(20), 2378–2380 (2004)
[75] W.C. Law, K.T. Yong, A. Baev, P.N. Prasad, "Sensitivity improved surface plasmon biosensor for cancer biomarker detection based on plasmonic enhancement", ACS nano 5(6), 4858–4864 (2011)
[76] M. Pu, L. Liu, W. Xue, Y. Ding, L.H. Frandsen, H. Ou, K. Yvind, and J.M. Hvam, "Tunable Microwave Phase Shifter Based on Silicon-on-Insulator Microring Resonator", IEEE Photon. Technol. Lett., vol. 22, no. 12, pp. 869–871, Jun. 2010.
[77] W.Y. Li et al., Dimers of Silver Nanospheres: Facile Synthesis and Their Use as Hot Spots for Surface-Enhanced Raman Scattering. Nano Letters 9(1): pp. 485–490, 2009.
[78] J.F. Li et al., Shell-isolated nanoparticle-enhanced Raman spectroscopy. Nature 464(7287): pp. 392–395, 2010.
[79] D.K. Lim et al., Highly uniform and reproducible surface-enhanced Raman scattering from DNA-tailorable nanoparticles with 1-nm interior gap, Nature Nanotechnology 6(7): pp. 452–460, 2011.
[80] C.G. Khoury, and T. Vo-Dinh, Gold Nanostars For Surface-Enhanced Raman Scattering: Synthesis, Characterization and Optimization, Journal of Physical Chemistry C 112(48): pp. 18849–18859. 2008.
[81] X.G. Deng et al., Single-Order, Subwavelength Resonant Nanograting as a Uniformly Hot Substrate for Surface-Enhanced Raman Spectroscopy, Nano Letters 10(5): pp. 1780–1786, 2010.
[82] R.G. Freeman et al., Self-assembled metal colloid monolayers: an approach to SERS substrates, Science 267(5204): pp. 1629–1632, 1995.
[83] Nicolas M.B. Perney, Jeremy J. Baumberg, Majd E. Zoorob, Martin D. B. Charlton, Sven Mahnkopf, and Caterina M. Netti, "Tuning localized plasmons in nanostructured substrates for surface-enhanced Raman scattering", Opt. Express 14, 847–857 (2006)
[84] M.L. Jin et al., "Large-area nanogap plasmon resonator arrays for plasmonics applications", Nanoscale 4(15), 4712–4718 (2012).
[85] H. Wang, C.S. Levin, and N.J. Halas, Nanosphere arrays with controlled sub-10-nm gaps as surface-enhanced Raman spectroscopy substrates, Journal of the American Chemical Society 127(43): pp. 14992–14993 (2005).
[86] Y. Chu, M.G. Banaee, and K.B. Crozier, Double-Resonance Plasmon Substrates for Surface-Enhanced Raman Scattering with Enhancement at Excitation and Stokes Frequencies, ACS Nano 4(5): pp. 2804–2810 (2010).
[87] M.G. Banaee and K.B. Crozier, Mixed Dimer Double-Resonance Substrates for Surface-Enhanced Raman Spectroscopy, ACS Nano 5(1): pp. 307–314 (2011).
[88] R. Rich, Y. Day, T. Morton, and D. Myszka, "High-resolution and high throughput protocols for measuring drug/human serum albumin interactions using Biacore", Analytical Biochemistry 296, 197-207 (2001)
[89] J.Hu, J. Hu, F. Luo, W. Li et al., "Design and validation of a low cost surface plasmon resonance bioanalyzer using microprocessors and a touch-screen monitor", Biosensors and Bioelectronics 24, 1974–1978 (2009)
[90] http://genalyte.com/technology-overview/
[91] W.R. Premasiri et al., Characterization of the Surface Enhanced Raman Scattering (SERS) of bacteria, Journal of Physical Chemistry B 109(1): p. 312–320 (2005).
[92] D.P. Cowcher, Y. Xu, and R. Goodacre, Portable, Quantitative Detection of Bacillus Bacterial Spores Using Surface-Enhanced Raman Scattering. Analytical Chemistry 85(6): p. 3297–3302 (2013).
[93] L.J. Lucas et al., Aggregation of nanoparticles in endosomes and lysosomes produces surface-enhanced Raman spectroscopy, Journal of Nanophotonics 9(1): 093094, 2015.
[94] D.P. Cowcher, Y. Xu, and R. Goodacre, Portable, Quantitative Detection of Bacillus Bacterial Spores Using Surface-Enhanced Raman Scattering, Analytical Chemistry, 2013. 85(6): p. 3297–

3302.

[95] R. Ahijado-Guzman et al., Surface-Enhanced Raman Scattering-Based Detection of the Interactions between the Essential Cell Division FtsZ Protein and Bacterial Membrane Elements, Acs Nano, 2012. **6**(8): p. 7514–7520.

[96] X. Yang et al., Highly Sensitive Detection of Proteins and Bacteria in Aqueous Solution Using Surface-Enhanced Raman Scattering and Optical Fibers. Analytical Chemistry 83(15): p. 5888–5894 (2011).

[97] Osorio-Roman, I.O., et al., Characterization of bacteria using its O-antigen with surface-enhanced Raman scattering. Analyst 135(8): p. 1997–2001 (2010).

[98] S. Yamazoe et al., Large-Area Surface-Enhanced Raman Spectroscopy Imaging of Brain Ischemia by Gold Nanoparticles Grown on Random Nanoarrays of Transparent Boehmite. Acs Nano 8(6): p. 5622–5632 (2014).